Chemical Engineering Journal 149 (2009) 221–231

Contents lists available at ScienceDirect

Chemical Engineering Journal

journal homepage: www.elsevier.com/locate/cej

Modeling the impacts of feed spacer geometry on reverse osmosis and nanofiltration processes

Greg Guillen, Eric M.V. Hoek*

Civil & Environmental Engineering Department and Water Technology Research Center, University of California, Los Angeles, CA 90095, USA

ARTICLE INFO

Article history:
Received 7 August 2008
Received in revised form 22 October 2008
Accepted 27 October 2008

Keywords:
Reverse osmosis
Nanofiltration
Computational fluid dynamics
Mass transfer
Water treatment

ABSTRACT

Maximizing mass transfer and minimizing hydraulic losses in spiral wound elements is critical for designing effective and efficient reverse osmosis (RO) and nanofiltration (NF) processes. Herein we describe a multi-scale modeling approach, which links microscopic and macroscopic transport phenomena in spiral wound elements. Model simulations elucidate the impacts of feed spacer geometry on full-scale RO/NF system performance considering four representative water treatment scenarios: (1) RO membranes used to desalt ocean water, (2) low-pressure RO membranes used to desalt brackish water, (3) ultra-low pressure RO membranes used to purify wastewater, and (4) NF membranes used to soften a hard, fresh water. According to model simulations, feed spacer geometry had little impact on mass transfer; hence, engineering spacers to improve concentration polarization, trans-membrane osmotic pressure, or product water quality may prove difficult and yield limited benefits. In contrast, thinner filaments spread further apart significantly reduced hydraulic losses with negligible impacts to mass transfer. In addition, a few non-circular filament shapes produced even lower hydraulic losses, which might prove beneficial for RO/NF treatment of low salinity waters where hydraulic losses through spiral wound elements contribute significantly to the total process energy consumption. In high salinity waters, improved spacer designs may not significantly reduce energy consumption because hydraulic losses through spiral wound elements are relatively small.

1. Introduction

Optimizing momentum and mass transfer in spiral wound elements is crucial for designing effective and efficient nanofiltration (NF) and reverse osmosis (RO) membrane processes. For example, poor mass transfer in NF/RO elements exacerbates concentration polarization, which increases osmotic losses, solute passage, and surface fouling phenomena [1–6]. Plastic mesh feed spacers are thought to improve mass transfer in spiral wound elements, but this improvement comes at the cost of increased hydraulic losses. Hence, efforts to understand the interplay between feed channel geometry, hydrodynamics, mass transfer, and pressure drop in NF/RO spiral wound elements comprised a significant component of membrane research for many years [7–12].

In principle, a better understanding of microscopic mass and momentum transfer in spacer-filled channels can improve spiral wound element design, product water quality, and energy efficiency of NF/RO processes. Numerous empirical correlations are available to describe mass and momentum transfer in open and spacer-filled channels [13,14]. These approximate analytical models provide channel-averaged descriptions that are easily leveraged in macroscopic models of full-scale NF/RO system performance [15]. An alternative modeling approach involves computational fluid dynamic (CFD) simulations, which rigorously describe microscopic transport phenomena [10,16–24]; however, it is difficult to translate CFD results into full-scale performance models.

The aim of this work is to develop a multi-scale model that links microscopic and macroscopic transport phenomena enabling rigorous assessment of full-scale process performance as a function of feed spacer geometry (filament size, shape, and separation). Microscopic transport is evaluated using a previously developed finite element-based numerical model of momentum and mass transfer in spacer-filled membrane feed channels [10]. Next, we fit the numerical results with empirical correlations for mass and momentum transfer. Finally, we incorporate the empirical correlations into a macroscopic model describing full-scale NF/RO process performance. Full-scale simulations elucidate potential impacts of feed spacer geometry on mass transfer, hydraulic losses, product water quality, and energy consumption in four representative NF/RO-based water purification scenarios.

* Corresponding author at: Civil & Environmental Engineering Department, University of California, 5732-G Boelter Hall, PO Box 951593, Los Angeles, CA 90095-1593, USA. Tel.: +1 310 206 3735; fax: +1 310 206 2222.
E-mail address: emvhoek@ucla.edu (E.M.V. Hoek).

1385-8947/$ – see front matter © 2008 Elsevier B.V. All rights reserved.
doi:10.1016/j.cej.2008.10.030

Nomenclature

a	vertical filament axis (m)
A_m	total membrane area (m^2)
b	horizontal filament axis (m)
c	solute concentration ($kg\,m^{-3}$)
c_0	source water solute concentration ($kg\,m^{-3}$)
c_b	bulk solute concentration ($kg\,m^{-3}$)
c_m	solute concentration at the membrane surface ($kg\,m^{-3}$)
c_p	local permeate solute concentration ($kg\,m^{-3}$)
C_p	average permeate solute concentration ($kg\,m^{-3}$)
CP_{avg}	channel average concentration polarization modulus
D	solute diffusivity ($m^2\,s^{-1}$)
d_f	feed spacer diameter (mm)
d_h	hydraulic diameter (mm)
f	channel average friction factor
f_{os}	osmotic coefficient ($Pa\,m^3\,kg^{-1}$)
h_c	channel height (mm)
J_s	total system solute flux ($kg\,m^{-2}\,s^{-1}$)
J_v	product water flux ($\mu m\,s^{-1}$)
k	channel average mass transfer coefficient ($m\,s^{-1}$)
L	total system length (m)
l_f	filament spacing (mm)
N_E	number of elements
p	pressure (Pa)
P_f	filament perimeter (m)
Q_f	feed water flowrate ($m^3\,s^{-1}$)
Q_p	total product water flowrate ($m^3\,s^{-1}$)
Re	Reynolds number
R_m	membrane resistance (m^{-1})
r_{obs}	observed solute rejection (%)
r_s	membrane intrinsic solute rejection (%)
Sc	Schmidt number
SEC	specific energy consumption ($kW\,h\,m^{-3}$)
Sh	Sherwood number
u	axial velocity ($m\,s^{-1}$)
u_0	superficial velocity ($m\,s^{-1}$)
v	local permeate velocity ($\mu m\,s^{-1}$)
v_{avg}	full-scale average product water flux ($\mu m\,s^{-1}$)
x	horizontal position coordinate (m)
X_f	filament cross-sectional area (m^2)
y	vertical position coordinate (m)
Y	system product water recovery (%)

Greek symbols

α	form drag coefficient
β	friction drag coefficient
γ	Reynolds exponent
Δp	applied pressure (Pa)
Δp_0	feed applied pressure (bar)
Δp_m	membrane pressure (Pa)
Δp_x	module pressure (Pa)
Δx	finite difference discretization (m)
$\Delta\pi_m$	osmotic pressure (Pa)
η_p	pump efficiency (%)
κ	mass transfer leading coefficient
λ	mass transfer exponential factor
μ	solution dynamic viscosity (Pa s)
ν	solution kinematic viscosity ($m^2\,s^{-1}$)
ρ	solution density ($kg\,m^{-3}$)

2. Model development

2.1. Full-scale NF/RO system performance

The macroscopic transport model outputs include global average product water quality in the form of system average permeate solute concentrations (C_p) and product water fluxes (J_v), as well as total product water recovered (Y) and specific energy consumed (SEC). System average product water flux is determined from

$$J_v = \frac{Q_p}{A_m} = \frac{\int_0^L v\ dx}{L}, \tag{1}$$

where Q_p is the total product water flow rate, A_m is the total membrane area, v is the local permeate velocity, x is the axial location, and L is the total system length. System average product water quality is determined from

$$C_p = \frac{J_s}{J_v} = \frac{\int_0^L vc_p\ dx}{\int_0^L v\,dx}. \tag{2}$$

Here, c_p is the local permeate solute concentration and J_s ($=Q_pC_p/A_m$) is the total system solute flux. System product water recovery is defined as the ratio of product and feed water volumetric flow rates

$$Y = \frac{Q_p}{Q_f} = \frac{\int_0^L v\ dx}{u_0 h_c} \tag{3}$$

Specific energy consumption is given as

$$\mathrm{SEC} = \frac{\Delta p_0}{Y\eta_p}, \tag{4}$$

where Δp_0 is the applied pressure and η_p is the pump efficiency. A pump efficiency of 85% is assumed for all simulations.

2.2. Macroscopic transport model

The full-scale RO/NF transport model of Song et al. [25] is extended here to include concentration polarization. The model is based on a series of differential mass and momentum balances and employs a forward difference numerical solution using the "solver tool" in Microsoft Excel to reproduce the desired product water recovery and flux. Applied pressure and feed velocity vary for each combination of source water and spacer geometry to meet the target product water recovery.

The local hydraulic pressure (Δp) is determined from

$$\Delta p_i = \Delta p_{i-1} - \frac{1}{2} f_{i-1}\rho u_{i-1}^2 \frac{\Delta x}{d_h}, \tag{5}$$

where f is the friction factor, ρ is the solution density, d_h is the hydraulic diameter, and Δx is the incremental distance. The cross-flow velocity, u, is defined as

$$u_i = u_{i-1} - 2v_i \frac{\Delta x}{h_c}, \tag{6}$$

where h_c is the channel height. Product water flux is given by the following equation:

$$v_i = \frac{\Delta p_{i-1} - \Delta\pi_{m.i-1}}{\mu R_m}, \tag{7}$$

where R_m is the membrane resistance, μ is the solution dynamic viscosity, and $\Delta\pi_m = f_{os}(c_m - c_p)$ is the osmotic pressure, where f_{os} is 78,000 $Pa\,m^3\,kg^{-1}$. The membrane surface solute concentration is defined as

$$c_m = c_b\left[1 - r_s + r_s\ \exp\left(-\frac{v_i}{k_i}\right)\right]^{-1}, \tag{8}$$

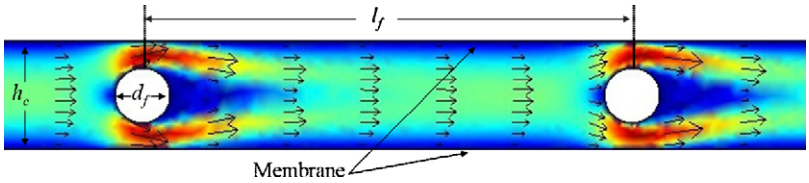

Fig. 1. Representative 2D geometry of spacer-filled channel section. The velocity field and velocity vector diagrams are overlaid.

where r_s is the local (real) solute rejection, k_i is the local mass transfer coefficient, and c_b is the local (bulk) solute concentration. Bulk solute concentration in the brine is determined from

$$c_{b,i} = \frac{u_{i-1}c_{b,i-1}}{u_i} - \frac{2\Delta x}{h_c}\frac{v_{i-1}c_{p,i-1}}{u_i}, \quad (9)$$

where c_p is the permeate solute concentration defined as $c_{p,i} = c_{m,i}(1 - r_s)$. Also, the local trans-membrane hydraulic pressure drop is calculated from $\Delta p_{m,i} = v_i \mu R_m$.

2.3. Microscopic transport model

A representative spacer-filled channel is presented in Fig. 1. In each finite element simulation, 8–15 spacers are located along the channel centerline at a filament spacing (l_f) of 2.25 mm or 4.50 mm, which are representative of commercial spiral wound elements cited in the literature and examined in our laboratory [7,15]. Filament diameter (d_f) varied from 0–0.35 mm, while channel length and height were fixed at 35 mm and 0.5 mm, respectively.

Different filament shapes, shown in Fig. 2, were modeled at a filament spacing of 4.50 mm. In both spacer size and spacer shape studies, the hydraulic diameter was fixed at 0.9 mm; hence, the shapes (drawn to scale in Fig. 2) offer a range of cross-sections. The selected hydraulic diameter was equal to that of a circular spacer with $d_f/h_c = 0.5$ for $h_c = 0.5$ mm and $l_f = 4.50$ mm. The ellipse and wing-shaped spacers are named according to their a:b axis ratio. For example, the 1:3 ellipse had an a:b axis ratio of 1:3. Wing-shaped spacers were constructed by pairing a half circle with an isosceles triangle. Each spacer was simulated as oriented in Fig. 2 with crossflow from left to right.

Inputs to model simulations included: superficial velocity at the channel inlet (u_0), permeate velocity (v), feed spacer filament diameter (d_f), filament length (l_f), channel height (h_c), intrinsic membrane solute rejection (r_s), and feed water solute concentration (c_0). Physical-chemical properties of the feed solution such as density (ρ), viscosity (μ), osmotic coefficient (f_{os}), and solute diffusivity (D) were assigned values of 10^3 kg m^{-3}, 10^{-3} Pa s, 78,000 Pa m^3 kg^{-1}, and 1.6×10^{-9} m^2 s^{-1}, respectively. A solute diffusivity of 8.5×10^{-10} m^2 s^{-1} was used for $CaCO_3$ in the fresh water NF scenario. Inlet superficial velocity was varied from 0.01–0.4 m s^{-1} to produce Reynolds numbers ranging from 10–400 in the crossflow channel. Parameters such as v, r_s, l_f, and d_f were also systematically varied from 4–16 μm s^{-1}, 50–99.7%, 2.25–4.50 mm, and 0–0.35 mm, respectively.

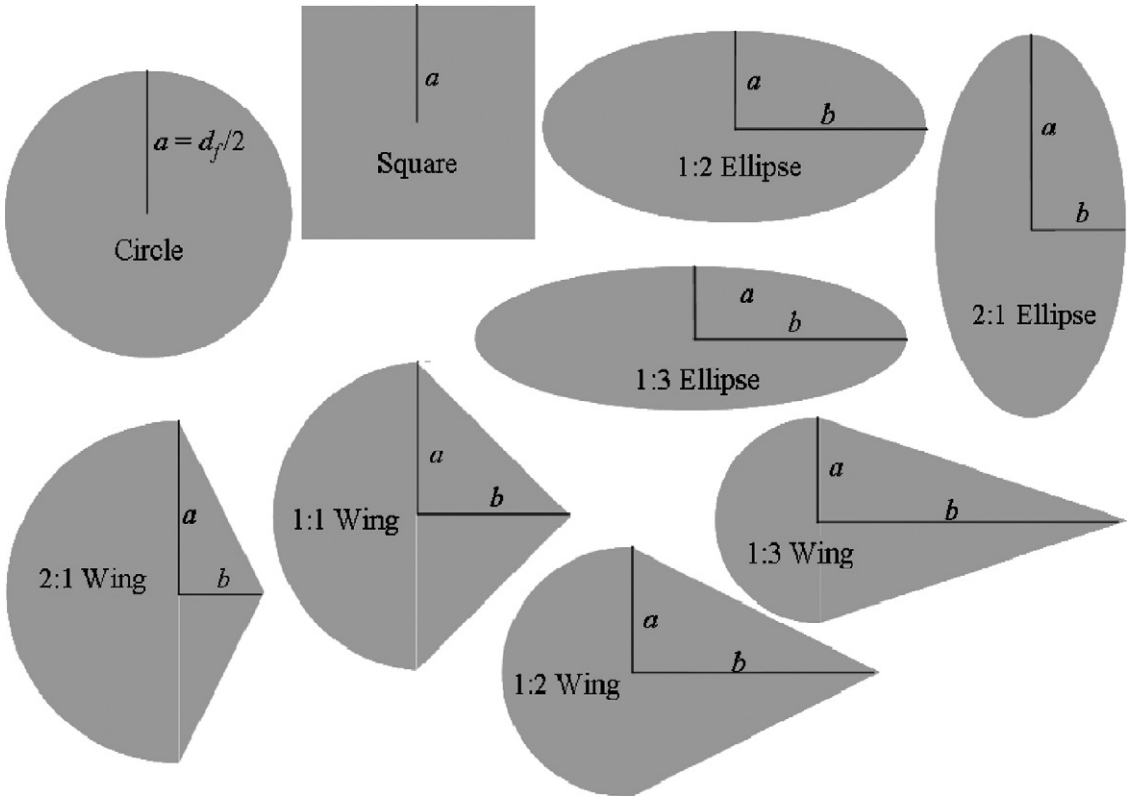

Fig. 2. Spacer shapes are drawn to scale and oriented (in simulations) as drawn above with crossflow from left to right. Ellipse and wing-shaped spacers are named by a:b axis ratios. For example, the 1:3 wing spacer has an a:b axis ratio of 1:3.

A commercial finite element solver (FEMLAB 3.0, Comsol Inc., Sweden) was used to spatially discretize the microscopic transport model geometry and solve the governing equations. Meshing procedures and numerical model details were originally developed by Subramani et al. [10], who found that the predicted solute concentration at the membrane surface was stable when more than 10,000 elements were used. Meshing refinements were often made manually near the membrane surface, and, as a general rule, each simulation in this study was conducted with at least 30,000 elements. Here, the equations of motion were solved to describe local pressure and velocity profiles. Boundary conditions were specified for feed channel inlet and outlet, and membrane and spacer surfaces. A parabolic velocity profile was specified for the feed channel inlet, and a pressure of 0 Pa was specified for the channel outlet. An axial velocity of 0 m s^{-1} and a constant permeate velocity were specified as boundary conditions for the membrane surfaces. A no-slip boundary condition was set for spacer surfaces.

Local velocities, thus determined, were inputs to solve the convection-diffusion equation, which gave local solute concentrations. Boundary conditions used to solve the convection-diffusion equation include a concentration at the channel inlet, mass flux at the membrane surfaces, insulation at the spacer surfaces, and convective mass flux at the channel outlet. Mass flux at the membrane surfaces is a function of permeate velocity, solute concentration at the membrane surface, and intrinsic membrane solute rejection. Model outputs included axial pressure drop per unit length and solute concentration along the length and cross-section of the channel. The channel average axial pressure drop was determined from the slope of the pressure profile over the channel length. The average concentration polarization factor (CP_{avg}) for the short channel section was determined by normalizing the local c_m value by the local bulk solute concentration (c_b) and integrating over the channel length [5].

2.4. Linking microscopic and macroscopic transport models

The procedure used to link microscopic and macroscopic transport is descried schematically in Fig. 3. Empirical correlations for the mass transfer coefficient and friction factor were developed from microscopic model simulations for each spacer configuration. These correlations were then used to predict the resulting mass transfer and hydraulic losses in the macroscopic transport model.

Channel average mass transfer coefficient (k) was calculated from the microscopically determined CP_{avg} using Eq. (8) as described previously [4]. A Sherwood number was then determined from

$$\mathrm{Sh} = k\frac{d_h}{D}. \tag{10}$$

Sherwood numbers were fit to a correlation of the form

$$\mathrm{Sh} = \kappa(Re\mathrm{Sc})^{\lambda}, \tag{11}$$

where the Schmidt number (Sc) is νD^{-1} and ν is the solution kinematic viscosity. Fitting parameters, κ and λ, were derived from least squares regressions of the calculated Sherwood numbers.

Open and spacer-filled channel friction factors were calculated from the pressure drops determined in microscopic transport simulations according to

$$f = -\frac{2d_h}{\rho u^2}\frac{dp}{dx}, \tag{12}$$

and fitted with a correlation of the form

$$f = \alpha + \frac{\beta}{Re^{\gamma}}. \tag{13}$$

Table 1
Operating parameters for model scenarios.

Scenario	SW-RO	HBW-RO	LBW-RO	FW-NF
c_0 (kg m^{-3})	32	5	1	0.3
r_s (%)	99.7	98.5	97.5	65/98
R_m (m^{-1})	5.5×10^{14}	1.5×10^{14}	10×10^{14}	5.5×10^{13}
v_{avg} (μm s^{-1})	4	8	6	12
Y (%)	50	75	80	90
N_E	5	8	$2 \times 5 + 5$	8

Here α, β, and γ were derived from least squares regression analyses on microscopic model results.

Two key parameters for expressing mass transfer and pressure losses are the Reynolds number ($\mathrm{Re} = ud_h/\nu$) and the hydraulic diameter. Hydraulic diameter (d_h) is calculated from

$$d_h = \frac{4 \text{ flow area}}{\text{wetted surface}} = \frac{4(l_f h_c - X_f)}{2l_f + P_f}. \tag{14}$$

Here l_f is the center-to-center distance between transverse spacer filaments, X_f is the projected cross-sectional area of a filament, and P_f is the filament perimeter. The perimeter of elliptical spacers is approximated from [26]

$$P_f = \pi(3(a+b) - \sqrt{(3a+b)(a+3b)}). \tag{15}$$

In numerical simulations, Reynolds number was varied from 10–400 and filament size (d_f/h_c) was varied from 0–0.7.

2.5. Full-scale scenarios simulated

Key characteristics describing the four water treatment scenarios used in full-scale NF/RO process simulations are summarized in Table 1. The scenarios include reverse osmosis desalination of seawater (SW-RO), highly brackish water (HBW-RO), and low brackish water (LBW-RO), plus nanofiltration of a fresh water source (FW-NF). The fresh water is modeled as 100 mg l^{-1} of monovalent ions and 200 mg l^{-1} divalent ions to capture the differential solute rejection and mass transfer that characterizes NF separations. Membranes were assigned separation performances characteristic of commercial seawater RO, brackish water RO, high flux RO, and true NF membranes. The nanofiltration membrane was given intrinsic rejections of 65 and 98% for monovalent and multivalent salts, respectively [27]. Nanofiltration and RO membrane separation performance values were chosen to represent general NF/RO membrane performance based on our experience and review of the literature [15,25,27–30].

System average fluxes were chosen to reflect current industry practices. Each element was modeled with a length of 1 m. The total system length was pre-determined assuming a maximum water recovery of 10–15% per element. Single stage configurations were used for SW-RO, HBW-RO, and FW-NF scenarios. A two stage configuration was used for the LBW scenario without a booster pump. Pressure vessels were simulated in a two-to-one array to boost mass transfer in the second stage. Each stage contained five elements in series. First stage recovery was 60% and the second stage recovery was 50%, giving a total system recovery of 80%.

3. Results and discussion

3.1. Insights derived from the microscopic model

The microscopic transport model describes concentration, pressure, and velocity profiles in a short section of a spacer-filled channel. Concentration and pressure profiles ($v = 6$ μm s^{-1}, $u_0 = 0.1$ m s^{-1}, and $r_s = 0.99$) for an open channel ($h_c = 0.5$ mm) and

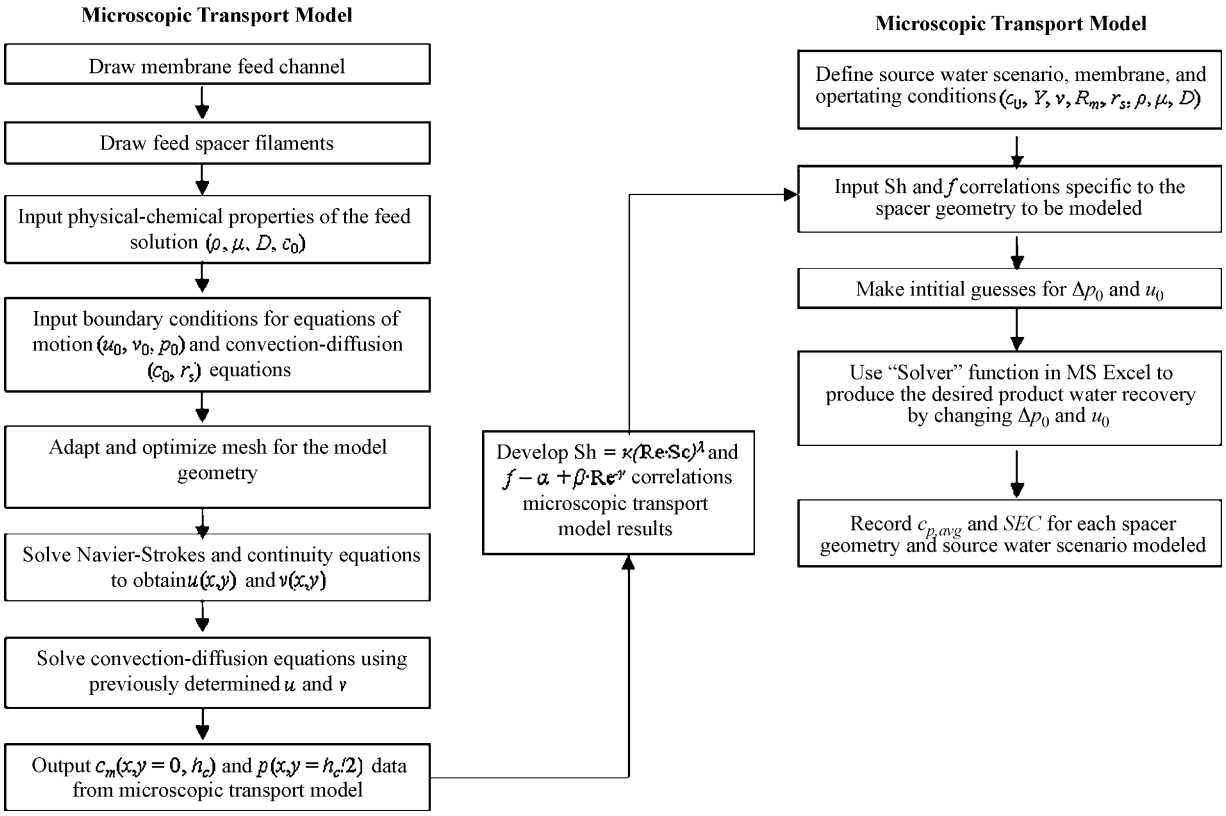

Fig. 3. Basic algorithm for linking microscopic and macroscopic transport models.

a spacer-filled channel (h_c = 0.5 mm, d_f/h_c = 0.5, and l_f = 2.25 mm) are plotted in Fig. 4. There is a sharp decrease in concentration and increase in pressure near each spacer. For the scenario depicted, spacers decrease concentration polarization by a few percent, but increase the axial pressure drop by about 500%.

Fig. 5 presents channel-average CP factors and axial pressure drops for circular filaments of different diameter and spacing. The greatest reduction in concentration polarization (~4% less than in an open channel) is achieved with the largest filament diameter (d_f/h_c = 0.7) spaced closely together (l_f = 2.25 mm). However, the axial pressure drop for this spacer configuration is about 1400% higher than that of an open channel. In general, larger filaments spaced closer together slightly enhance mass transfer, but dramatically increase hydraulic pressure losses.

3.2. Correlating spacer geometry with mass transfer

Sherwood numbers are plotted against Reynolds number in Fig. 6. Sherwood numbers were determined for crossflow channels by varying inlet velocity, permeation velocity, and spacer geometry

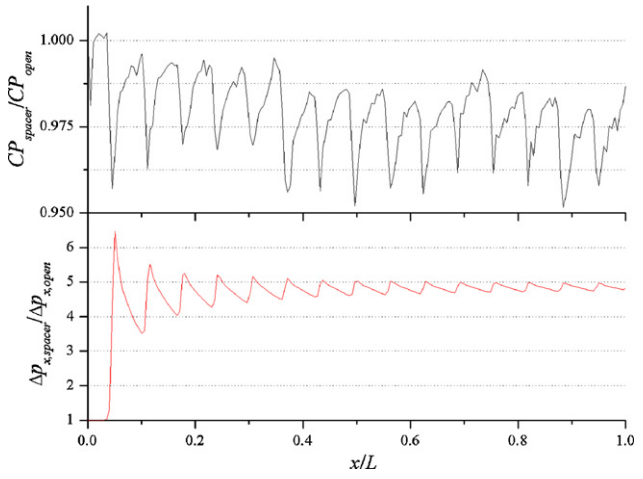

Fig. 4. Normalized concentration polarization factor and pressure drop results (l_f = 2.25 mm, h_c = 0.5 mm, d_f/h_c = 0.5, v = 6 μm s^{-1}, u_0 = 0.1 m s^{-1}, Re = 85, Sc = 620, and r_s = 0.99).

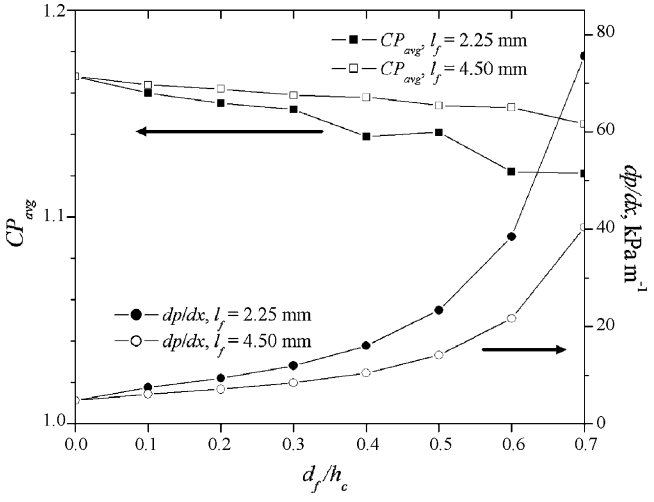

Fig. 5. Channel average concentration polarization modulus and axial pressure drop for different circular spacer diameters and filament spacings. Other common simulation parameters include v = 6 μm s^{-1}, u_0 = 0.1 m s^{-1}, Re = 85, Sc = 620, and h_c = 0.5 mm.

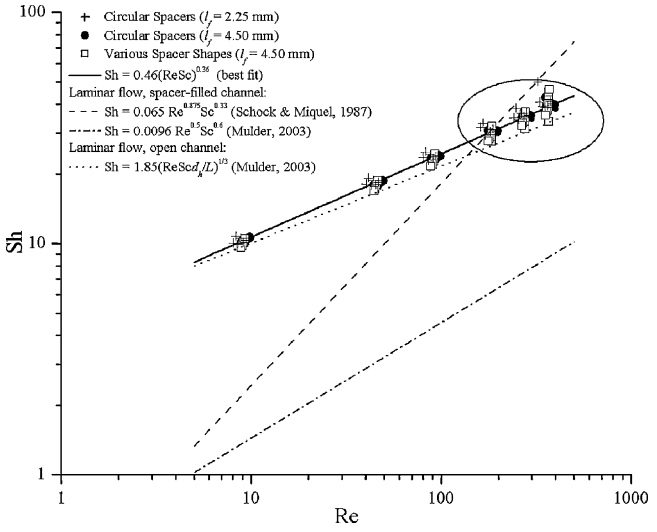

Fig. 6. Sherwood number versus Reynolds number for $v = 4$–$6\,\mu m\,s^{-1}$, $r_s = 0.50$–0.997, Sc = 620, and $h_c = 0.5$ mm. Symbols (+, ●, □) represent microscopic model results. Solid line represents correlations developed from model results. Dashed lines represent previously published Sherwood number correlations.

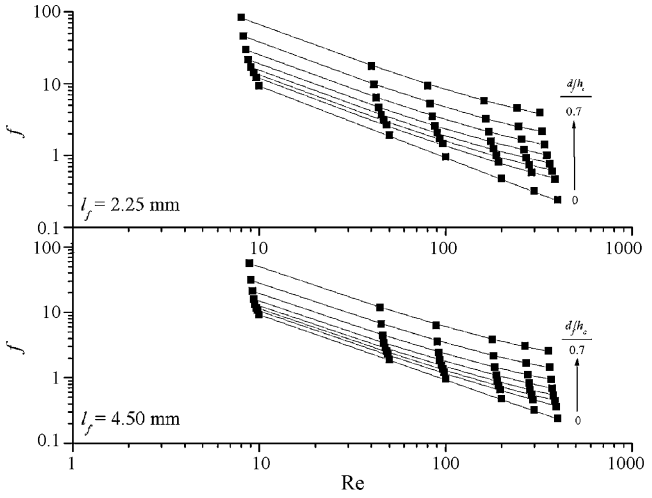

Fig. 7. Friction factor for circular spacers of different size and spacing as a function of Reynolds number with $v = 4$–$6\,\mu m\,s^{-1}$, $r_s = 0.50$–0.997, Sc = 620, and $h_c = 0.5$ mm. Symbols (■) represent microscopic model results; lines represent correlations developed from microscopic model results.

(filament size, shape, and separation distance). Numerically determined Sherwood numbers were fitted with a simple function of Reynolds number and Schmidt number by systematically varying κ and λ values. The Sherwood number was negligibly influenced by water flux and solute rejection in the ranges of 4–16 $\mu m\,s^{-1}$ (8–32 gfd) and 50–99.7%, respectively. All Sherwood number values were reasonably fit ($R^2 = 0.983$) by a single linear regression with κ and λ values equal to 0.46 and 0.36, respectively. The largest deviation (±20%) between microscale model results and this correlation occurred above Reynolds numbers of 200.

Previously published Sherwood number correlations [7,31] are plotted alongside the microscopic model results as indicated in Fig. 6. Empirical Sherwood number correlations for spiral wound elements did not agree with microscopic model results across the wider range of Reynolds numbers, but agreed reasonably well for practical Reynolds numbers (200–400). The region circled in Fig. 6 represents the Reynolds number range at which full-scale NF/RO processes are thought to operate [15]. Sherwood numbers for laminar flow in open channels are also plotted in Fig. 6 using a channel length (L) of 3.5 cm and hydraulic diameter of 0.9 mm, which is the average hydraulic diameter based on all filaments modeled in this study. This correlation slightly under-predicts, but agrees well with microscopic model results.

3.3. Correlating spacer geometry with hydraulic losses

Finite element results and correlations for circular spacer friction factors are plotted in Fig. 7. A filament spacing of 2.25 mm produced more pressure loss than did a filament spacing of 4.50 mm. The friction factor correlation given in Eq. (13) follows the general form of the Ergun equation, which describes pressure drop in porous media from the sum of the Kozeny–Carman and Burke–Plumber equations [32,33]. Friction factor scaled inversely with Reynolds number ($0.94 < \gamma < 1.06$) for all spacers. However, each spacer produced unique form (α) and friction (β) drag coefficients, which are summarized in Table 2. The friction factor correlations plotted in Fig. 7 use γ values of 1. Friction factor correlations for each spacer diameter and filament spacing agree well with microscale model results in the range of modeled Reynolds number ($R^2 = 1.00$). The variation in α and β values highlights the importance of spacer size and separation in spiral wound element design.

Table 2
Drag coefficients for circle spacers.

d_f/h_c	l_f = 2.25 mm			l_f = 4.50 mm		
	d_h (mm)	α	β	d_h (mm)	α	β
0	1.00	0	93.08	1.00	0	93.08
0.1	0.96	0.18	116.31	0.98	0.11	104.56
0.2	0.93	0.28	129.42	0.96	0.16	112.34
0.3	0.89	0.37	149.53	0.94	0.22	124.98
0.4	0.85	0.50	183.82	0.92	0.30	147.32
0.5	0.81	0.69	244.17	0.90	0.42	189.29
0.6	0.77	1.04	365.22	0.88	0.66	275.31
0.7	0.73	1.81	644.96	0.85	1.18	488.30

The friction factor is plotted in Fig. 8 against Reynolds number for spacer filaments of different shapes. The range of α and β values for differently shaped spacers was large, and thus, unique values were recorded for each shape. Form and friction drag coefficients plus effective cross-sections (a/h_c) are provided in Table 3. The friction factor correlations plotted in Fig. 8 all use γ values of 1. Friction factor correlations for each spacer shape agree well with microscale model results in the range of modeled Reynolds number ($R^2 = 1.00$). Spacer shapes with smaller cross-sections normal to crossflow (i.e., a:b 1:3) exhibited lower friction factors, while those shapes with larger cross-sections produced higher friction factors. The square spacer friction factor is slightly less than that of the circular spacer because it occupies a smaller cross-section of the

Table 3
Normalized cross-section and drag coefficients for different spacer shapes.

Shape	a/h_c	α	β
1:3 ellipse	0.13	0.13	128.24
1:2 ellipse	0.17	0.17	141.24
1:3 wing	0.18	0.19	135.56
Square	0.20	0.42	176.99
1:2 wing	0.22	0.29	152.16
Circle	0.25	0.42	189.29
1:1 wing	0.27	0.59	190.96
2:1 wing	0.30	0.91	236.73
2:1 ellipse	0.33	1.44	315.63

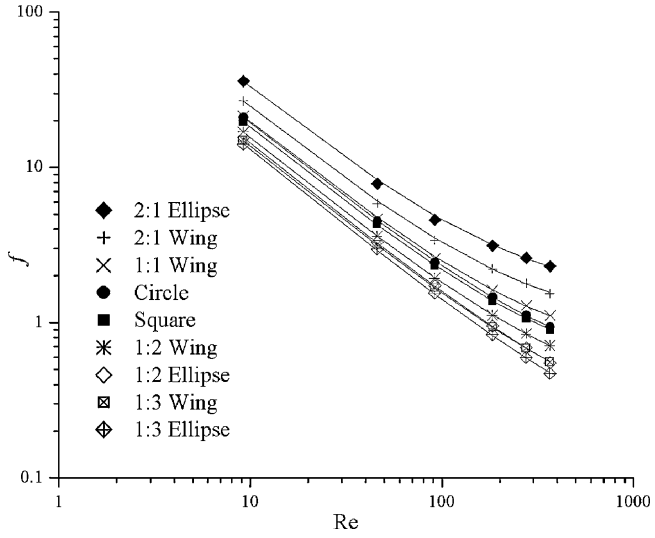

Fig. 8. Friction factor correlations for various spacer shapes as a function of Reynolds number with $l_f = 4.50$ mm, $v = 4$–6 μm s^{-1}, $r_s = 0.50$–0.997, Sc = 620, and $h_c = 0.5$ mm.

flow channel ($a/h_c = 0.20$ for square, $a/h_c = 0.25$ for circle). Spacer orientation also affected momentum transfer. The 1:2 ellipse and 2:1 ellipse are the same shape rotated 90°. The 2:1 ellipse produced about three times larger axial pressure drop than the 1:2 ellipse.

3.4. Impacts of spacer geometry on full-scale NF/RO system performance

Sherwood number and friction factor correlations derived from finite element simulations are used in macroscopic model simulations to assess the potential impacts of spacer geometry on full-scale NF/RO system performance. Key system performance parameters are product water quality and specific energy consumption. In the model, the feed channel Sherwood number influences both parameters, while the friction factor affects only the energy consumption. The four simulated scenarios represent practical water treatment applications with different water qualities, membrane properties, system designs, and operating conditions. The goal is to understand the relative importance of spacer design for these four common NF/RO water treatment scenarios. Normalized concentration and pressure profiles for the four source water scenarios are plotted in Figs. 9–12. Feed channels contain circular spacers with $d_f/h_c = 0.5$, $h_c = 0.5$ mm, and $l_f = 2.25$ mm.

Retentate and permeate concentrations are normalized by each stream's respective concentration at the inlet (c_0). Permeate concentration is influenced by concentration polarization, whereas the retentate concentration reported is for the bulk solution. The reported pressures are normalized by the applied pressure. The profile dubbed "osmotic" is the osmotic pressure difference between retentate and permeate streams. The pressure profile titled "polarization" is the excess osmotic pressure due to concentration polarization. The "membrane" pressure is the hydraulic pressure drop across the membrane, while "friction" pressure is the hydraulic pressure drop due to frictional losses through the series of spiral wound elements. Average contributions of membrane, osmotic, friction, and polarization pressures are assessed at the system midpoint denoted by a shaded region in Figs. 9–12.

Representative concentration and pressure profiles for seawater RO system containing circular feed spacers is presented in Fig. 9. Normalized retentate and permeate concentrations both increased to about 2 for the simulated water recovery of 50% and intrinsic solute rejection of 99.7%. At the system midpoint, the different pressure drops ranked in the following order: osmotic (59%) > membrane (35%) > polarization (5%) > friction (1%). Global average product water solute concentration for this scenario was 145 mg l^{-1} giving an observed solute rejection of 99.5% for the system. The total applied pressure and specific energy consumption for this scenario was 62.7 bar and 4.1 kW h m^{-3}, respectively. With energy recovery the net energy consumption would be approximately 2.2 kW h m^{-3} for a savings of about 46% [34].

Normalized concentration and pressure profiles are presented in Fig. 10 for low-pressure reverse osmosis membranes treating highly brackish water. Normalized retentate and permeate concentrations increased to a value of approximately 4 at 75% water recovery and intrinsic solute rejection of 98.5%. Factors contributing to the applied pressure decreased in the following order: membrane (50%) > osmotic (34%) > friction (11%) > polarization (5%). In contrast to the seawater scenario, membrane resistance was the dominant factor—even when operating low energy membranes at high recovery. Global average product water solute concentration was 157 mg l^{-1} giving an observed rejection of 96.9% for the system. The total applied pressure and specific energy consumption for this scenario were 24.0 bar and 1.05 kW h m^{-3}, respectively. Energy recovery is not frequently used in brackish water desalination, but specific energy consumption could be reduced to about 0.85 kW h m^{-3} for a savings of about 18%.

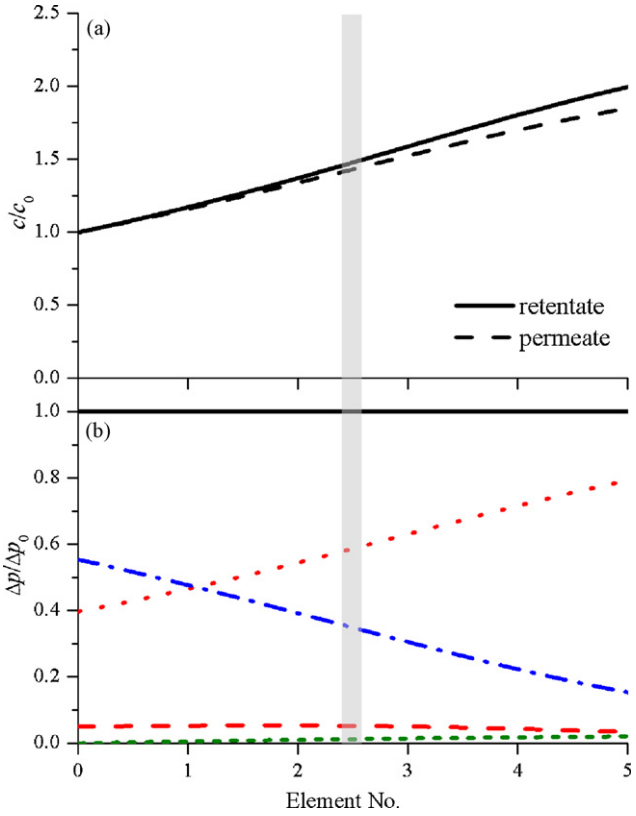

Fig. 9. Normalized concentration (a) and pressure (b) profiles for SW-RO scenario with $l_f = 2.25$ mm, $d_f/h_c = 0.5$, $h_c = 0.5$ mm, and $\Delta p_0 = 62.7$ bar. In (a), retentate and permeate concentrations are normalized by each stream's respective concentration at the inlet (c_0). In (b), applied (▬), membrane (▬ ▪ ▬), osmotic (● ● ● ●), polarization (▬ ▬ ▬), and friction (▬ ▬ ▬) pressures are normalized by Δp_0.

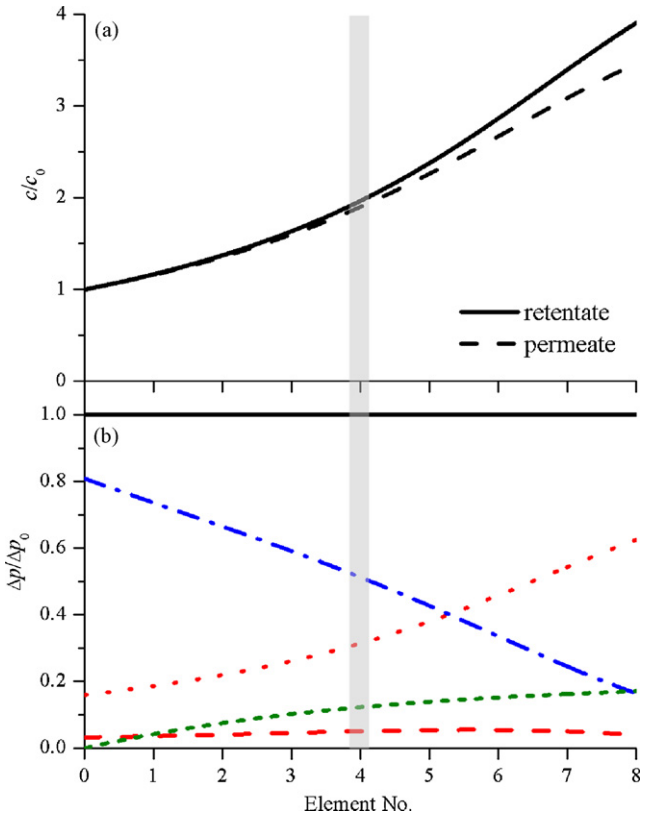

Fig. 10. Normalized concentration (a) and pressure (b) profiles for HBW-RO scenario with l_f = 2.25 mm, d_f/h_c = 0.5, h_c = 0.5 mm, and Δp_0 = 24.0 bar. In (a), retentate and permeate concentrations are normalized by each stream's respective concentration at the inlet (c_0). In (b), applied (▬), membrane (▬ ▪ ▬), osmotic (● ● ● ●), polarization (▬ ▬ ▬), and friction (▬ ▬ ▬) pressures are normalized by Δp_0.

Representative pressure and concentration profiles are presented in Fig. 11 for ultra-low pressure RO membranes treating slightly brackish water, perhaps representative of the dissolved solids content in a municipal wastewater [15]. Normalized concentrations increase to a value of approximately 5 at a water recovery of 80% and a intrinsic solute rejection of 97.5%. On average, the factors contributing to the applied pressure decreased in the following order: membrane (57%) > osmotic (21%) > friction (20%) > polarization (2%). Hydraulic losses through the elements contributed about the same as osmotic pressure losses for this scenario. Average product water solute concentration for this scenario was 55 mg l^{-1} producing an observed rejection of 94.5%. The total applied pressure and specific energy consumption for this scenario were 9.6 bar and 0.945 kW h m^{-3}, respectively.

In a previous study of a pilot scale RO wastewater reclamation plant, hydraulic losses accounted for about 57% of total applied pressure (at startup) [15]; however, this system was designed in a three-stage cascading 3:2:1 array, which was not optimized for hydraulic losses. Interestingly, frictional hydraulic losses increased by about 10% due to fouling, but just before the plant was shut down for cleaning frictional losses accounted for only 38% of the total applied pressure.

Representative concentration and pressure profiles are presented in Fig. 12 for nanofiltration membranes treating a fresh surface water. Normalized concentrations increase to a value of approximately 7 in the retentate stream and 4 in the permeate stream at a recovery of 90% and intrinsic rejections of 65 and 98%, respectively, for monovalent and divalent ions. The differences in the rise of permeate and retentate concentrations are due to the differential solute rejection. On average, factors contributing to the applied pressure decreased in the following order: membrane (60%) > friction (30%) > osmotic (7%) > polarization (3%). Average product water solute concentrations were 67 and 14 mg l^{-1} for monovalent and divalent ions, respectively, producing observed solute rejections of 32.6 and 93.1%. The observed total dissolved solids observed rejection was 73%. The total applied pressure and specific energy consumption for this scenario were 10.6 bar and 0.386 kW h m^{-3}, respectively. Similar results were reported in a pilot study by Dow FilmTec [35]. Total applied pressure was higher for this scenario than for the ultra-low pressure RO membranes treating slightly brackish water due to the higher flux in the nanofiltration scenario (12 μm s^{-1} compared to 6 μm s^{-1} for FW-NF and LBW-RO scenarios, respectively). Higher flux increases hydraulic pressure loss across the membrane. Also, the nanofiltration scenario operates at a higher recovery (90%) than the ultra-low pressure RO scenario (80%), which leads to higher solute concentration and osmotic pressure.

3.5. Implications for improving specific energy consumption

Observed solute rejection (r_{obs}) and normalized specific energy consumption are plotted against d_f/h_c in Fig. 13 for circular spacers and all four treatment scenarios. For each spacer shape, specific energy consumption values are normalized by that determined for an open channel, while the actual SEC results are provided in Table 4. Solute rejection is virtually unaffected by spacer geometry, and the lowest specific energy consumption for all scenarios is an open feed channel. This trend was universal for the ladder-

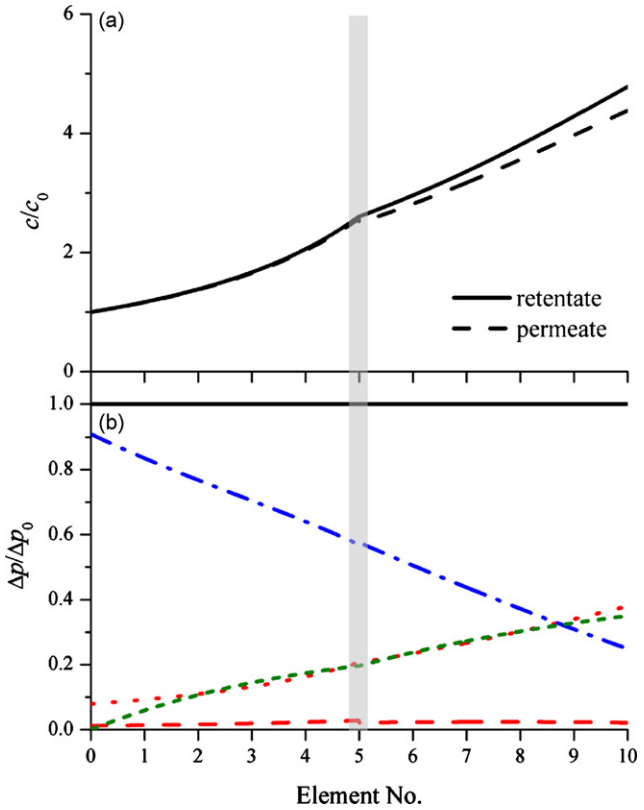

Fig. 11. Normalized concentration (a) and pressure (b) profiles for LBW-RO scenario with l_f = 2.25 mm, d_f/h_c = 0.5, h_c = 0.5 mm, and Δp_0 = 9.6 bar. In (a), retentate and permeate concentrations are normalized by each stream's respective concentration at the inlet (c_0). In (b), applied (▬), membrane (▬ ▪ ▬), osmotic (● ● ● ●), polarization (▬ ▬ ▬), and friction (▬ ▬ ▬) pressures are normalized by Δp_0.

Table 4
Specific energy consumption (kW h m^{-3}) for circular spacers.

d_f/h_c	Scenario l_f (mm)	FW-NF 2.25	4.50	LBW-RO 2.25	4.50	HBW-RO 2.25	4.50	SW-RO 2.25	4.50
0		0.2955		0.6646		0.945		4.081	
0.1		0.3139	0.3058	0.6817	0.6783	0.961	0.954	4.082	4.082
0.2		0.3260	0.3118	0.6905	0.6783	0.972	0.959	4.081	4.081
0.3		0.3402	0.3199	0.7002	0.6840	0.985	0.966	4.082	4.081
0.4		0.3622	0.3320	0.7164	0.6933	1.007	0.978	4.086	4.083
0.5		0.3974	0.3520	0.7459	0.7112	1.045	0.998	4.098	4.089
0.6		0.4623	0.3910	0.8091	0.7494	1.119	1.040	4.127	4.105
0.7		0.5948	0.4752	0.9520	0.8399	1.287	1.137	4.206	4.147

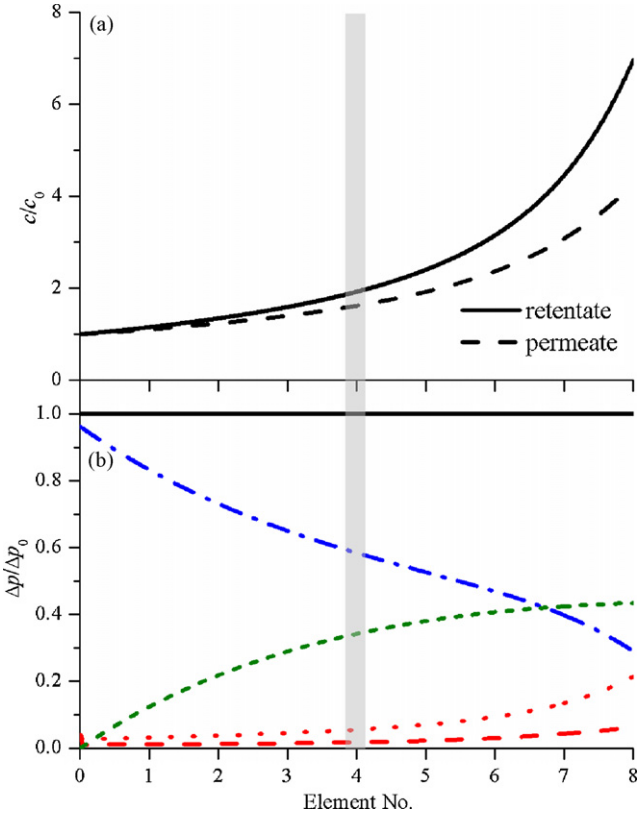

Fig. 12. Normalized concentration (a) and pressure (b) profiles for FW-NF scenario with l_f = 2.25 mm, d_f/h_c = 0.5, h_c = 0.5 mm, and Δp_0 = 10.6 bar. In (a), retentate and permeate concentrations are normalized by each stream's respective concentration at the inlet (c_0). In (b), applied (▬), membrane (▬ ▪ ▬), osmotic (● ● ● ●), polarization (▬ ▬ ▬), and friction (▬ ▬ ▬) pressures are normalized by Δp_0.

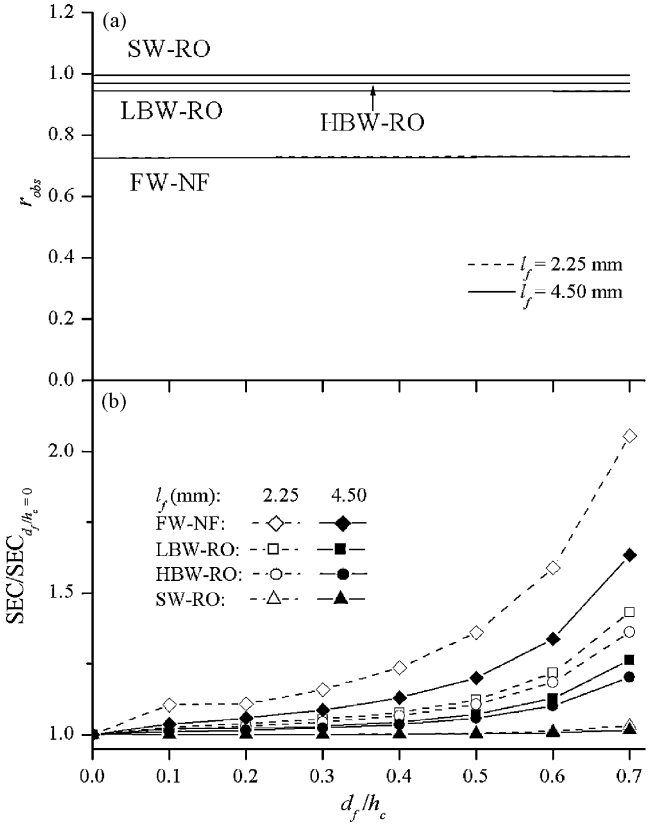

Fig. 13. Observed solute rejection (a) and normalized specific energy consumption (b) as a function of filament size and spacing for each scenario with h_c = 0.5 mm.

type spacer orientation simulated, but it is not clear how this result translates for the more common diamond-type spacer orientation. The most significant result is observed for the fresh water NF scenario, where the open channel produced a specific energy consumption 50% lower than the largest spacer (d_f/h_c = 0.7) and smallest filament spacing (l_f = 2.25 mm).

Observed solute rejection and normalized SEC are plotted for each spacer shape in Fig. 14 for the four water treatment scenarios. Actual specific energy consumption values are also reported in Table 5. Spacers of various shapes are plotted in order of increasing normalized cross-section (a/h_c). Spacer shape had virtually no impact on observed solute rejection. Of the spacer shapes modeled, the 1:3 elliptical spacer filaments produced the lowest energy consumption. This was true for all four scenarios. In each scenario, the circle spacer fell in the mid-range of specific energy consumptions, with many filament shapes yielding lower specific energy consumptions. The 2:1 elliptical spacer resulted in the highest SEC for all scenarios. These model results suggest that novel spacer designs would have very little benefit for high TDS waters like seawater, while significant energy savings might be realized for NF/RO treatment of low TDS feed waters by optimizing spacer geometry for frictional losses.

Table 5
Specific energy consumption (kW h m^{-3}) for different spacer shapes.

Spacer shape	a/h_c	FW-NF	LBW-RO	HBW-RO	SW-RO
1:3 ellipse	0.13	0.3176	0.6784	0.964	4.075
1:2 ellipse	0.17	0.3236	0.6830	0.970	4.078
1:3 wing	0.18	0.3236	0.6844	0.970	4.078
Square	0.20	0.3491	0.7071	0.995	4.087
1:2 wing	0.22	0.3345	0.6939	0.980	4.082
Circle	0.25	0.3974	0.7459	1.045	4.089
1:1 wing	0.27	0.3634	0.7210	1.009	4.092
2:1 wing	0.30	0.3937	0.7522	1.040	4.104
2:1 ellipse	0.33	0.4412	0.8032	1.091	4.125

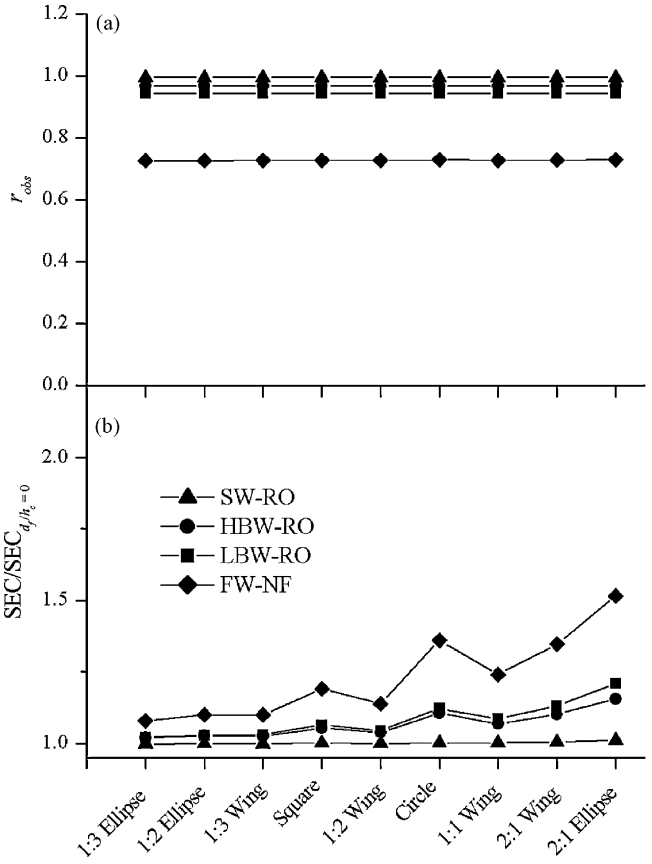

Fig. 14. Observed solute rejection (a) and normalized specific energy consumption (b) for all spacer shapes modeled with $l_f = 4.50$ mm, $h_c = 0.5$ mm, and $d_h = 0.9$ mm. Spacers are plotted in order of increasing normalized cross-section (a/h_c) for each scenario.

4. Conclusions

A new multi-scale modeling approach utilized finite element simulations of momentum and mass transfer in spacer-filled channels to develop mass transfer and friction factor correlations, which were then used in a macroscopic model of full-scale NF/RO process performance. Hence, the impacts of microscopic transport were translated into system level outcomes for the first time. From this model study, we conclude the following.

- Friction-related hydraulic losses are dramatically more sensitive to spacer geometry than are mass-transfer related osmotic losses.
- Feed spacer geometry has little impact on product water quality for the spacer geometries, membrane properties, and water treatment scenarios considered.
- Nanofiltration and ultra-low pressure reverse osmosis spiral wound elements might be improved by designing spacers to minimize hydraulic losses.
- Mass transfer and hydraulic losses in ocean and brackish water RO elements may not significantly improve with advanced spacer designs.

This work suggests that theoretical attempts to improve NF/RO spiral wound elements should begin with a fundamental understanding of the practical separation process. A given spacer geometry had very different impacts on the four applications considered. Although these model results appear qualitatively reasonable, additional studies should be pursued to evaluate other spacer orientations (i.e., diamond-type) and to better understand the role of spiral wound element feed spacers in membrane fouling and cleaning.

Acknowledgements

Financial support for this work was provided by the UCLA Cota-Robles fund and graduate student opportunity award. We also thank Dr. Arun Subramani of MWH for valuable discussions regarding finite element-based CFD simulations.

References

[1] M. Uchymiak, A. Rahardianto, E. Lyster, J. Glater, Y. Cohen, A novel RO ex situ scale observation detector (EXSOD) for mineral scale characterization and early detection, J. Membr. Sci. 291 (2007) 86–95.
[2] S. Bhattacharjee, G.M. Johnston, A model of membrane fouling by salt precipitation from multicomponent ionic mixtures in crossflow nanofiltration, Environ. Eng. Sci. 19 (2002) 399–412.
[3] E.M.V. Hoek, A.S. Kim, M. Elimelech, Influence of crossflow membrane filter geometry and shear rate on colloidal fouling in reverse osmosis and nanofiltration separations, Environ. Eng. Sci. 19 (2002) 357–372.
[4] E.M.V. Hoek, M. Elimelech, Cake-enhanced concentration polarization: a new fouling mechanism for salt-rejecting membranes, Environ. Sci. Technol. 37 (2003) 5581–5588.
[5] S. Kim, E.M.V. Hoek, Modeling concentration polarization in reverse osmosis processes, Desalination 186 (2005) 111–128.
[6] R.Y. Ning, T.L. Troyer, Colloidal fouling of RO membranes following MF/UF in the reclamation of municipal wastewater, Desalination 208 (2007) 232–237.
[7] G. Schock, A. Miquel, Mass-transfer and pressure loss in spiral wound modules, Desalination 64 (1987) 339–352.
[8] S.K. Karode, A. Kumar, Flow visualization through spacer filled channels by computational fluid dynamics I. Pressure drop and shear rate calculations for flat sheet geometry, J. Membr. Sci. 193 (2001) 69–84.
[9] D. Dendukuri, S.K. Karode, A. Kumar, Flow visualization through spacer filled channels by computational fluid dynamics-II. Improved feed spacer designs, J. Membr. Sci. 249 (2005) 41–49.
[10] A. Subramani, S. Kim, E.M.V. Hoek, Pressure, flow, and concentration profiles in open and spacer-filled membrane channels, J. Membr. Sci. 277 (2006) 7–17.
[11] V. Geraldes, M.D. Afonso, Prediction of the concentration polarization in the nanofiltration/reverse osmosis of dilute multi-ionic solutions, J. Membr. Sci. 300 (2007) 20–27.
[12] V. Geraldes, V. Semiao, M.N. de Pinho, Flow management in nanofiltration spiral wound modules with ladder-type spacers, J. Membr. Sci. 203 (2002) 87–102.
[13] V. Gekas, B. Hallstrom, Mass-transfer in the membrane concentration polarization layer under turbulent cross flow. 1. Critical literature-review and adaptation of existing Sherwood correlations to membrane operations, J. Membr. Sci. 30 (1987) 153–170.
[14] V. Geraldes, M.N. de Pinho, Mass transfer coefficient determination method for high-recovery pressure-driven membrane modules, Desalination 195 (2006) 69–77.
[15] E.M.V. Hoek, J. Allred, T. Knoell, B.H. Jeong, Modeling the effects of fouling on full-scale reverse osmosis processes, J. Membr. Sci. 314 (2008) 33–49.
[16] S. Chellam, M.R. Wiesner, Evaluation of crossflow filtration models based on shear-induced diffusion and particle adhesion: complications induced by feed suspension polydispersivity, J. Membr. Sci. 138 (1998) 83–97.
[17] J. Marriott, E. Sorensen, A general approach to modelling membrane modules, Chem. Eng. Sci. 58 (2003) 4975–4990.
[18] G.R. Shetty, R.R. Sharma, S. Chellam, Scale-up methodology for municipal water nanofiltration based on permeate water quality, Environ. Eng. Sci. 19 (2002) 545–562.
[19] L.F. Song, S.C. Yu, Concentration polarization in cross-flow reverse osmosis, AIChE J. 45 (1999) 921–928.
[20] D. Van Gauwbergen, J. Baeyens, Modeling and scaleup of reverse osmosis separation, Environ. Eng. Sci. 19 (2002) 37–45.
[21] J.L.C. Santos, V. Geraldes, S. Velizarov, J.G. Crespo, Investigation of flow patterns and mass transfer in membrane module channels filled with flow-aligned spacers using computational fluid dynamics (CFD), J. Membr. Sci. 305 (2007) 103–117.
[22] A. Alexiadis, D.E. Wiley, A. Vishnoi, R.H.K. Lee, D.F. Fletcher, J. Bao, CFD modelling of reverse osmosis membrane flow and validation with experimental results, Desalination 217 (2007) 242–250.
[23] D.E. Wiley, D.F. Fletcher, Techniques for computational fluid dynamics modelling of flow in membrane channels, J. Membr. Sci. 211 (2003) 127–137.
[24] Z. Cao, D.E. Wiley, A.G. Fane, CFD simulations of net-type turbulence promoters in a narrow channel, J. Membr. Sci. 185 (2001) 157–176.
[25] L. Song, S. Hong, J.Y. Hu, S.L. Ong, W.J. Ng, Simulations of full-scale reverse osmosis membrane process, J. Environ. Eng. ASCE 128 (2002) 960–966.
[26] G.H. Hardy, P.V.S. Seshu Aiyar, B.M. Wilson, Collected Papers of Srinivasa Ramanujan, Chelsea Publishing Company, New York, NY, 1962.
[27] R. Rautenbach, A. Groschl, Separation potential of nanofiltration membranes, Desalination 77 (1990) 73–84.

[28] C.J. Harrison, Y.A. Le Gouellec, R.C. Cheng, A.E. Childress, Bench-scale testing of nanofiltration for seawater desalination, J. Environ. Eng. ASCE 133 (2007) 1004–1014.
[29] N. Fujiwara, H. Matsuyama, High recovery system in seawater reverse osmosis plants, J. Appl. Polym. Sci. 108 (2008) 3403–3410.
[30] M. Pontie, H. Dach, J. Leparc, M. Hafsi, A. Lhassani, Novel approach combining physico-chemical characterizations and mass transfer modelling of nanofiltration and low pressure reverse osmosis membranes for brackish water desalination intensification, Desalination 221 (2008) 174–191.
[31] M. Mulder, Basic Principles of Membrane Technology, Kluwer Academic Publishers, Dordrecht, The Netherlands, 2003, pp. 421–426.
[32] S. Ergun, Fluid flow through packed columns, Chem. Eng. Prog. 48 (1952) 89–94.
[33] N. de Nevers, Fluid Mechanics for Chemical Engineers, McGraw-Hill Inc., New York, NY, 1991, pp. 412–419.
[34] R.L. Stover, Seawater reverse osmosis with isobaric energy recovery devices, Desalination 203 (2007) 168–175.
[35] J. Johnson, M. Hallan, Municipal groundwater softening with an energy-saving RO feed spacer, in: Proceedings of the North American Membranes Society, Orlando, FL, USA, 2007.